Three-dimensional crustal structure in central Taiwan from gravity inversion with a parallel genetic algorithm

Jian Zhang*[‡], Chi-Yuen Wang*, Yaolin Shi[‡], Yongen Cai**, Wu-Cheng Chi*, Douglas Dreger*, Win-Bin Cheng[§], and Yen-Horng Yuan[‡‡]

ABSTRACT

The genetic algorithm method is combined with the finite-element method for the first time as an alternative method to invert gravity anomaly data for reconstructing the 3D density structure in the subsurface. The method provides a global search in the model space for all acceptable models. The computational efficiency is significantly improved by storing the coefficient matrix and using it in all forward calculations, then by dividing the region of interest into many subregions and applying parallel processing to the subregions. Central Taiwan, a geologically complex region, is used as an example to demonstrate the utility of the method. A crustal block 120×150 km^2 in area and 34 km in thickness is represented by a finite-element model of 76 500 cubic elements, each $2 \times 2 \times 2$ km^3 in size. An initial density model is reconstructed from the regional 3D tomographic seismic velocity using an empirical relation between velocity and density. The difference between the calculated and the observed gravity anomaly (i.e., the residual anomaly) shows an elongated minimum of large magnitude that extends along the axis of the Taiwan mountain belt. Among the interpretive models tested, the best model shows a crustal root extending to depths of 50 to 60 km beneath the axis of the Western Central and Eastern Central Ranges with a density contrast of 400 or 500 kg/m^3 across the Moho. Both predictions appear to be supported by independent seismological and laboratory evidence.

INTRODUCTON

An important set of geophysical data for investigating the subsurface density structure of an area is the gravity anomaly.

The classical method in geophysical inversion that uses gradient calculation (e.g., R. L. Parker, 1972; Oldenburg, 1974) may yield results trapped in a local minimum and thus biased by the assumed initial model (e.g., Camacho et al., 2002; Silva et al., 2002). With the advent of fast computers, alternative methods based upon a stochastic approach, such as the genetic algorithm, have become popular.

The genetic algorithm is designed for solving a variety of optimization problems. It is a stochastic search technique that imposes the Darwinian principle of survival of the fittest in biological evolution on a population of individual models. The main feature is to assign higher probabilities of reproduction to the individual models with better fit to produce better solutions. A large number of initial models are first generated. Each model consists of a series of chromosomes, with each chromosome representing a cell within the model mesh. When prior information is not available, the starting population may be randomly initialized. These models are evaluated according to a set of given constraints and are allowed to evolve by the principle of natural selection through many generations. The method is robust and effective in finding optimal models that satisfy the given constraints, and it provides a global search in the model space for all acceptable models (Goldberg and Richardson, 1987; Goldberg, 1989; Shi, 1992; B. P. Parker, 1999). Furthermore, it may be adaptable to parallel processing to increase computational efficiency.

Even with the power of today's computers, the application of the genetic algorithm to geophysical inversion in complex geologic regions is limited by available computer resources. Two factors contribute to the genetic algorithm's demand on computer resources: (1) the large number of parameters needed to maximize the resolution of the model and (2) the amount of computation required in the forward calculation to evaluate the objective function of each individual model. For complex geologic regions, the required computer time in the forward

computation may become so substantial to render the application of the genetic algorithm impractical. Cai and Wang (personal communication, 2003) have used a new finite-element approach to significantly improve the efficiency in the forward computation. Here, we exploit these aspects of the genetic algorithm with parallel processing in the gravity inversion of the 3D subsurface density structure, and we illustrate this method by applying it to the study of the crust in central Taiwan.

METHOD

Forward calculation

In a Cartesian coordinate system, the general 3D expression for calculating the gravity anomaly (along the z-axis) resulting from subsurface anomalous masses is

$$\Delta g(x, y, z) = G \iiint_V \Delta \rho(\xi, \eta, \zeta)$$
$$\times \frac{(z - \zeta)}{[(x - \xi)^2 + (y - \eta)^2 + (z - \zeta)^2]^{3/2}} \, d\xi \, d\eta \, d\zeta, \quad (1)$$

where G is the gravitational constant, V the subsurface region of interest, $\Delta\rho$ the anomalous density with respect to some reference density (x, y, z) and (ξ, η, ζ)—the coordinates of the field station and the anomalous density. Approximate expressions for direct integration based on expression (1) have been developed for 2D bodies (e.g., Talwani et al., 1959) and 3D bodies in Cartesian coordinates (e.g., Blakely, 1995) and in spherical coordinates (Johnson and Litehiser, 1972).

Alternatively, one may calculate the gravity anomaly by solving the following Poisson's differential equation for the gravitational potential ϕ with appropriate boundary conditions,

$$\nabla^2 \phi = -4\pi G \Delta \rho, \quad (2)$$

and then applying the relation

$$\Delta g(x, y, z) = -\left(\frac{\partial \phi}{\partial z}\right). \quad (3)$$

In assigning the boundary conditions, one would ideally assign $\phi = 0$ at infinite distance. In numerical analysis, however, one may approximate this condition by surrounding the source region with many empty layers (i.e., $\Delta\rho = 0$) and assigning $\phi = 0$ on the outermost boundary of the empty layers.

Equation (2) has the same form as the differential equations in many field problems such as heat flow, diffusion, and groundwater flow. Hence, many numerical techniques, such as the finite-element method, may be used in gravity modeling of subsurface density in regions with complex structures. The finite-element method has been widely used in engineering analyses and discussed in many textbooks (e.g., Zienkiewicz and Taylor, 1989; Bathe, 1996). Briefly, the method begins with the discretization of the region of study into small elements; the continuum solution is then replaced by discrete and approximate solutions at the element nodes, i.e., $\phi_1, \phi_2, \ldots, \phi_n$, where n is the total number of element nodes. The governing equation (2) may then be transformed to a set of linear algebraic equations (Zienkiewicz and Taylor, 1988, p. 264):

$$\mathbf{K}\Phi + \mathbf{Q} = 0, \quad (4)$$

where

$$\Phi = [\phi_1, \phi_2, \ldots, \phi_n]^T, \quad (5)$$

$$\mathbf{K} = \sum_{e=1}^{m} \int_{V_e} (\nabla N)^T \nabla N dV_e, \quad (6)$$

$$\mathbf{Q} = -4\pi G \sum_{e=1}^{m} \int_{V_e} N^T \Delta \rho(x, y, z) \, dV_e. \quad (7)$$

Here, N is an interpolation vector (or the shape function in finite-element terminology) of the element, which is a function of position only; ∇ is the gradient operator vector; e denotes the element number; m denotes the total number of elements; V_e is the volume of the element e; and $\rho(x, y, z)$ is the density distribution in the element, interpolated from the densities on the element nodes. Since the $\mathbf{K}$ matrix is a function of the shape function and the finite-element grid, which do not change throughout the gravity modeling, it can be computed once, stored, and used in all forward computations. In essence, the finite-element procedure reduces the second-order partial differential equation (2) to a set of algebraic equations (4). Solving equation (4) we get ϕ_i; applying equation (3), we get the gravity anomaly.

Inverse modeling with parallel genetic algorithm

At the start of the genetic algorithm cycle, random values are assigned to the strings in all models of a generation. The models evolve through three basic processes: reproduction, crossover, and mutation. Models are selected according to their fitness, evaluated with a misfit function discussed below. Selected models are paired into parents and are allowed to generate offsprings. Crossover involves the partial exchange of model characteristics, and mutation involves the occasional random alteration of the value at a string position. Both crossover and mutation enrich the diversity in the genetic pool. In particular, mutation prevents early convergence by introducing new genes into the population, essentially expanding the gene pool and allowing other regions of the solution space to be explored. Finally, the offspring are evaluated for their fitness. Once these values have been assigned, the offspring are placed back into the population, often replacing their parents, to create the next generation of potential solutions. Once the new generation is created, the genetic algorithm cycle is repeated. The process is continued until convergence is achieved.

The rate of convergence in the genetic algorithm depends on the population size in a generation and the rates of crossover and mutation. The population size, crossover rate, and mutation rate are problem dependent and may be varied according to the performance of the genetic algorithm. Numerical experiments by other authors (Goldberg, 1989; Shi, 1992; Parker, 1999) suggest that, for best results, the population size should be between 32 and 128, the crossover rate between 0.8 and 1, and the mutation rate between 0.001 and 0.02.

Several misfit functions may be used; each has some advantages and some disadvantages (e.g., Hjelt, 1992). A widely used function is the sum of the squares of the misfit (e.g., Mansanne and Schoenauer, 2002), i.e.,

$$f = \sum_{i=1}^{n} \left(\Delta g_i^o - \Delta g_i^c\right)^2, \quad (8)$$

where Δg_i^o and Δg_i^c are, respectively, the observed and the calculated gravity anomalies at the ith gravity station and n is the total number of gravity stations. For this study we choose to use the square root of this function, i.e.,

$$f' = \left\{ \sum_{i=1}^{n} \left(\Delta g_i^o - \Delta g_i^c \right)^2 \right\}^{1/2}. \tag{9}$$

The relative fitness among the models in a given generation is used as an index for assigning the relative chance of survival among the models.

For geophysical problems with a very large number of parameters, we may divide the subsurface region into N subregions and apply parallel processing to the subregions. To ensure a broad spectrum of solutions from the subregions, a loose constraint may be used at this stage. The best models from the subregions are then reassembled in a final search with a tighter constraint. Numerical experiments show that the parallel process so described improves the computational efficiency by a factor of $\sim N$.

We carry out a numerical experiment to verify whether the genetic algorithm procedure may effectively recover the subsurface masses from gravity anomaly data. We first form an arbitrary mass in the subsurface and calculate its gravity anomaly; we then use the calculated gravity anomaly as the synthetic data in the genetic algorithm inversion to reconstruct the subsurface mass. To this end, we build a finite-element grid to represent a subsurface inverted pyramid of 21×21 km^2 in area and 12 km in depth (Figure 1a). The grid has 5292 cubic finite-element elements, each $1 \times 1 \times 1$ km^3 in size; a uniform density of 1000 kg/m^3 is assigned to each element. The gravity anomaly calculated from this mass is shown in Figure 1b and is taken as the data in the inverse problem. In the genetic algorithm inversion, we assume that the density contrast is known and that the depth and the thickness of the layer in which the mass is embedded are given. We start by randomly assigning a density of either 0 or 1000 kg/m^3 to the elements in the layer and use a population size of 32, a crossover rate of 0.9, and a mutation rate of 0.001.

The inverted mass body is shown in Figure 1c; the calculated gravity for the inverted mass body is shown in Figure 1d. Comparing Figures 1a and 1c, we see that the genetic algorithm inversion has effectively recovered the subsurface mass. The difference between Figures 1a and 1c is given in Figure 1e; it shows two small pieces of the original mass are missing from the inverted mass. These missing pieces occur deep within the mass where the resolving power of the gravity data is relatively low. The difference between Figures 1b and 1d is given in Figure 1f, which shows that the amplitude of the difference between the calculated gravity of the inverted mass and the synthetic data is about 1.5×10^{-5} m/s^2 (i.e., 1.5 mGal), or 2.5% of the amplitude of the gravity in the synthetic data. We conclude that the genetic algorithm inversion of gravity data may be an effective means of finding the subsurface masses if correct specifications are given on the density contrast between the mass and its surroundings and on the depth of the layer in which the mass is embedded.

APPLICATION TO CENTRAL TAIWAN

As an example, we apply the genetic algorithm gravity inversion to central Taiwan, a geologically complex region. We first summarize the relevant geologic and geophysical information. From this information we construct an initial density model and calculate its gravity anomaly. The differences between the calculated and the observed anomalies are used in calculating the misfit function (9), which in turn is used in the genetic algorithm inversion. Finally, we present and discuss the results of the inversion.

Geologic setting

Taiwan is a mountainous island that rises locally to $\sim$4 km. It was formed after the late Cenozoic, with the oblique collision between the Luzon volcanic arc on the Philippine Sea plate and the China continental margin (Teng, 1990). The location of the collision has migrated from north to south (Suppe, 1987), with the suture zone marked by the Longitudinal Valley (Figure 2). The prevailing structural trend in Taiwan is that of an elongated arc convex to the west. Several structural belts have been differentiated. These are, from west to east, the coastal plain, floored by a pre-Tertiary block-faulted basement and covered by flat-lying Cenozoic sedimentary sequences (Teng 1990); the
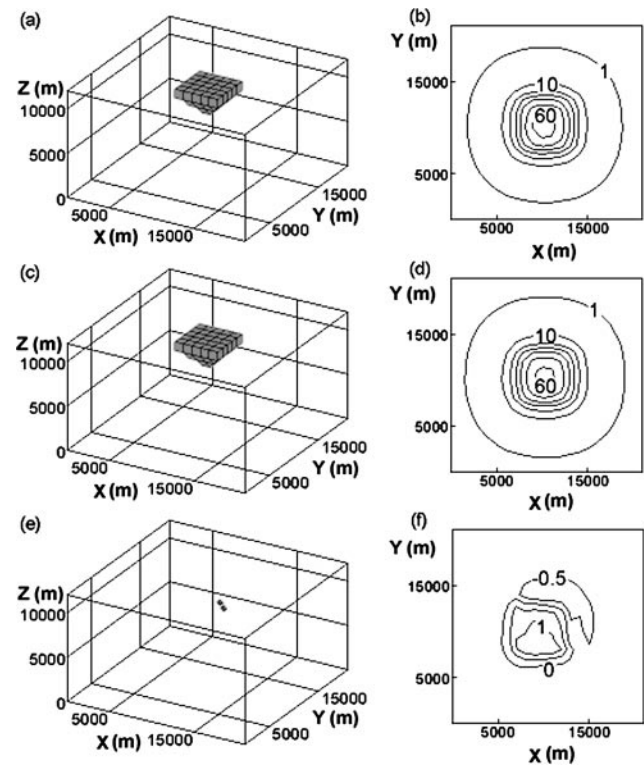

Figure 1. (a) Finite-element grid for a subsurface region in which a mass in the shape of an inverted pyramid is implemented. The base of the pyramid, with a surface area of 5×5 km^2, is at a depth of 1 km, the height of the pyramid is 3 km, and the density of the pyramid is 1000 kg/m^3. Density elsewhere is zero. (b) Calculated gravity for the mass. This is used as the synthetic data in the genetic algorithm inversion. (c) Recovered mass from the genetic algorithm inversion of the synthetic data. (d) Calculated gravity for the inverted mass. (e) Difference between the synthetic mass in (a) and the inverted mass in (c). (f) Difference between the synthetic data and the calculated gravity for the inverted mass. Numbers on contours are in units of 10^{-5} m/s^2 (i.e., mGal).

western foothills, consisting of a fold-and-thrust belt of sedimentary rocks; the Western Central Range, consisting of slates; the Eastern Central Range, pre-Tertiary schists and metamorphic limestone (Ho, 1988); and the Coastal Range along the eastern margin of the island, representing the deformed and uplifted Luzon arc (Ho, 1988). Northeast of Taiwan, the Philippine Sea plate subducts northward beneath the Ryukyu arc–trench system (Teng, 1990). South of Taiwan, the oceanic crust of the South China Sea is subducting eastward beneath the Philippine Sea plate at the Luzon arc (Angelier et al., 1995). In this study we focus on the central section of Taiwan (Figure 2) away from the subduction zones.

Geophysical constraints

Three-dimensional tomographic P-wave velocity structures for Taiwan have been published by Rau and Wu (1995) and Cheng (2000). Since the density and the seismic wave velocity of crustal rocks are closely related (e.g., Birch, 1961; Christensen and Mooney, 1995), it is reasonable to construct an initial density model for the crust from the available seismic velocity. In this study we use Cheng's tomographic velocity model because it was specifically designed for central Taiwan. The model was based on a simultaneous inversion of 24 230 P-wave traveltimes from 2582 events, as recorded by the Taiwan Central Weather Bureau's seismic network. Application of a checkerboard test (Humphreys and Clayton, 1988) showed good resolution at a grid spacing of 10 km (Cheng, 2000).

This velocity model is converted to an initial density model by using an empirical relationship between velocity and density. The latter is obtained by fitting the experimental data presented in Dobrin and Savit (1988) for both crystalline and sedimentary rocks at $V_p \leq 2$ km/s:

$$\rho = 1.5325 + 0.3148V_p - 0.0384V_p^2 + 0.0032V_p^3, \quad (10)$$

where ρ is density in 10^{-3} kg/m^3 and V_p is the P-wave velocity in kilometers per second. Equation (10) is consistent with the relation by Christensen and Mooney (1995) that is specific for crystalline rocks, but equation (10) can also be applied to sedimentary rocks, which are important for this study. The resulting density model is given in Figure 3. Since Cheng's velocity model is restricted in the upper 34 km, the initial density model is also restricted in the upper 34 km.

The published Bouguer gravity anomaly of Taiwan (Yen et al., 1995) is used in the present genetic algorithm inversion. The gravity data were based on more than 600 evenly distributed measurements over the island, with an average distance of 7 km between the stations. Estimated error, including instrumental drift, tidal disturbances, and points of gravity measurements in the terrain corrections in mountainous areas, is $\pm 2.5 \times 10^{-5}$ m/s^2 (i.e., 2.5 mGal) (Tsai, 1999). The determination of the regional trend in the gravity data is highly subjective and is a topic of current debate (e.g., Camacho et al., 2002). Generally, the regional trend is given by the lower frequency components in the gravity data and represents the deeper density effect. After filtering out the lower frequencies, the remaining data represent the density in the crust. We experimented with different polynomials and found that, even though the magnitude of the anomaly changed with different polynomial fits, the major character in the gravity anomaly remained unchanged. In the study we used the simplest correction, i.e., removal of the linear trend from the original data. The resulting Bouguer gravity anomaly (Figure 4a) shows an elongated area of minimum gravity that lies along the boundary between the Western Central Range and the Western Foothills.

Next we remove the effect of the known structures from the gravity anomaly. The contribution of the initial density model to the gravity anomaly is calculated with the finite-element method, as described earlier. We represent the crustal block in central Taiwan by a finite-element mesh of 76 500 elements, each $2 \times 2 \times 2$ km^3 in size. Since the average density does not contribute to gravity anomaly, we subtract the average density of each horizontal layer from the initial density model, leaving only the density difference. The calculated gravity anomaly for the density model is presented in Figure 4b. It shows negative
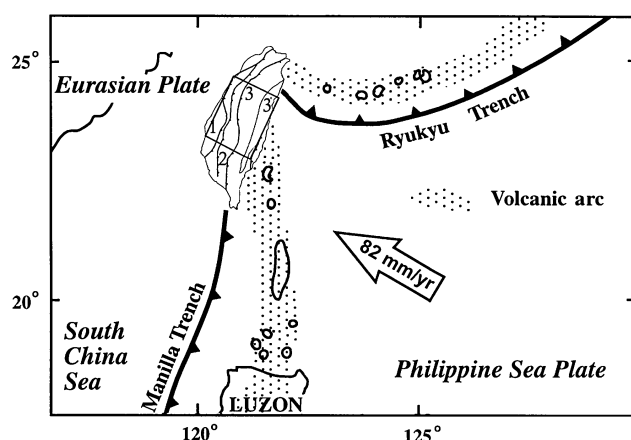

Figure 2. Location map of the study area (within the square box marked over Taiwan). The numbered major structural units are (1) coastal plain, (2) Western Foothills, and (3) Eastern and Western Central Ranges. The eastern boundary of the ranges, marked by a fault, is the longitudinal valley. The sliver east of the longitudinal valley is the coastal range.
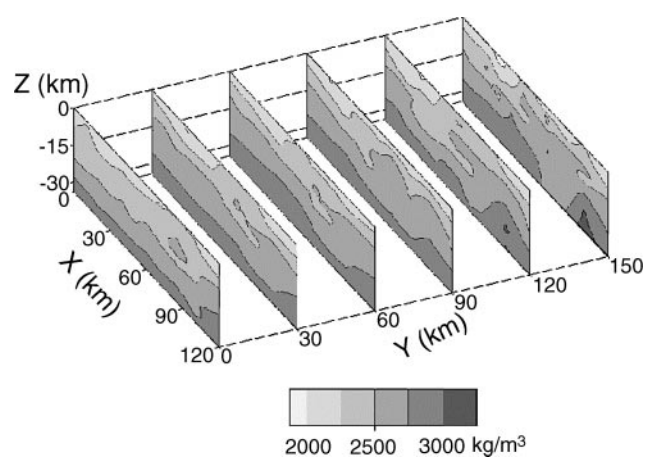

Figure 3. Initial density model converted from Cheng's (2000) tomographic seismic velocity with equation (6). Note the occurrence of relatively low-density sedimentary basins on the west side of the island and the occurrence of relatively high-density crust on the east.

values on the western side of the island, reflecting the relatively low density of the sedimentary rocks, and positive values on the eastern side, reflecting the relatively higher density of the metamorphic rocks and the crystalline basement.

Subtracting the contribution from the upper 34 km (Figure 4b) from the gravity anomaly in Figure 4a, we have the residual anomaly, as shown in Figure 4c. Subtracting the contribution of the upper 34 km from the Bouguer gravity anomaly shifts the location of the gravity minimum eastward, from the boundary between the Western Central Range and the Western Foothills (Figure 4a) to the axis of the Western Central Range and the Eastern Central Range in the north (Figure 4c). The most interesting feature in Figure 4c is an elongated arc of negative gravity anomaly that runs along the axis of the ranges. This anomaly must be from an unknown structure not represented in Cheng's tomographic seismic velocity; it thus provides the basic data for geophysical inversion.

GENETIC ALGORITHM INVERSION AND RESULTS

Because of the trade-off between density contrast and depth in gravity modeling, an infinite number of models may satisfy the gravity data. We use the misfit function in the model space
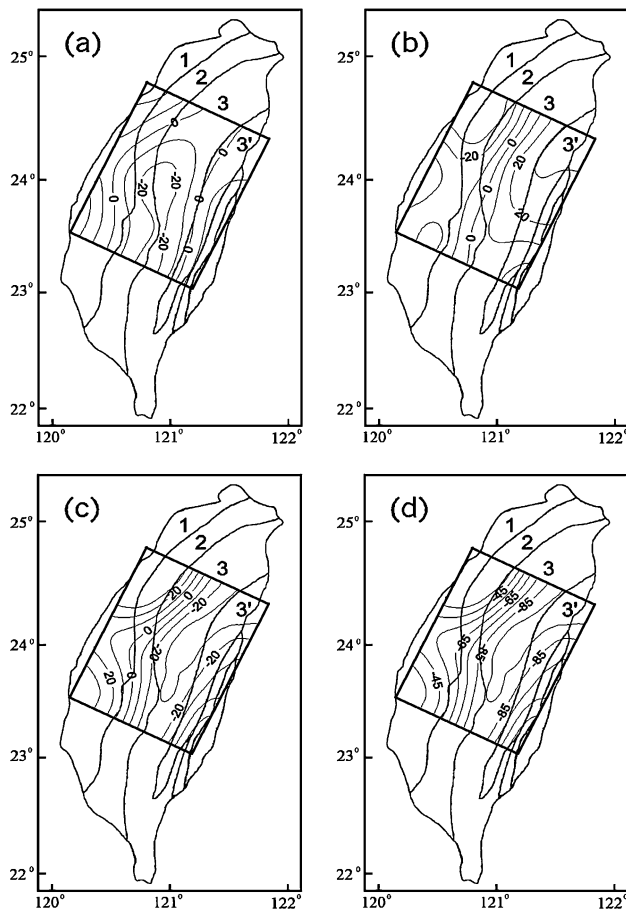

Figure 4. (a) Bouguer gravity anomaly of the study area, after removal of linear regional trends from the data (Yen et al., 1995), overlaid on outlines of major structure units of Taiwan. (b) Gravity anomaly calculated from density model in Figure 3. (c) Residual gravity anomaly, i.e., difference between (a) and (b). (d) Same as (c), except a constant 65×10^{-5} m/s^2 (i.e., 65 mGal) is subtracted (see text for explanation).

to guide the genetic algorithm inversion in search of the best models for the crustal density structure in central Taiwan. Two end-member cases are considered in this study: In the first case, we assume that the residual gravity anomaly is attributable to the undulations of the Moho below 34 km, creating a laterally heterogeneous mass distribution. In the second case, we assume that the density below 34 km is laterally uniform and the residual gravity anomaly is the result of a density structure in the upper 34 km, not represented in the initial density model.

In each case, it is important not only to find a solution but also to know the shape of the misfit function in the model space near the solution. By fixing all parameters except one and changing the unfixed parameters, we can calculate the corresponding changes in the misfit function (5). By plotting the misfit function against the parameter, we can determine whether the local minimum is located in a deep well or in a gentle valley. If it is in a deep well, the solution is good at least near this point. If, instead, it is in a gentle valley, then the data have low resolution for the parameter near this point. This approach does not solve the problem of uniqueness in the inversion, but at least we can get some insight to the nature of the local minimums.

To increase the computational efficiency, we divide the study region into 20 subregions (Figure 5) and apply the genetic algorithm to the subregions in parallel. Relevant gravity measurements that fall immediately outside of the boundary of the study area (<10 km) are included in the inversion. The best models from the subregions are then assembled in a complete search. As before, we choose a population size of 32 models, a crossover rate of 0.9, and a mutation rate of 0.001.

Case 1: Moho undulations

Here we invert the gravity data to determine the Moho undulation below 34 km, assuming that the density in the upper 34 km is fixed by the initial model. If we choose the mantle density as the reference in the inversion, the crustal densities will appear negative and the residual anomaly in Figure 4c will shift toward negative by a constant value. The magnitude of this density contrast shift is a function of the depth of the Moho. If the Moho undulation occurs immediately beneath 34 km, this negative shift is 65×10^{-5} m/s^2; the resulting anomaly is shown in Figure 4d.

The density contrast across the Moho must be determined. Because of the trade-off between density contrast and Moho
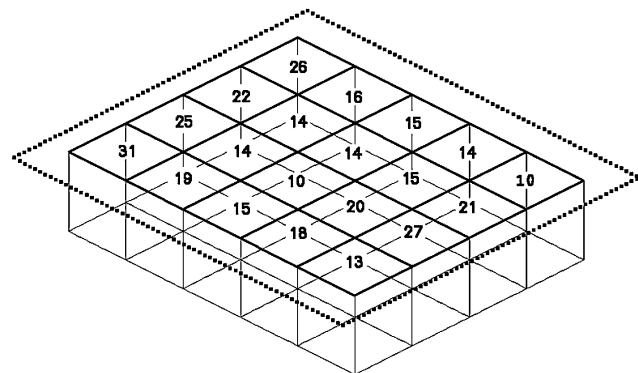

Figure 5. Subdivisions of the study region into columns for parallel genetic algorithm inversion (see text for detail). Numbers in each square mark the number of gravity measurements used in parallel inversion for density in the respective column.

depth, we determine the density contrast by examining the shape of the misfit function in the model space of the two variables: the Moho density contrast and the maximum Moho depth (Figure 6). We construct the configuration of the misfit function by independently changing the Moho density contrast from 200 to 600 kg/m^3, at steps of 100 kg/m^3, and the maximum Moho depth from 40 to 70 km, at steps of 5 km. To save computer time, we use only ten model generations for each point in the model space. The misfit function so constructed (Figure 6) shows an elongated belt of relative minimum. Two isolated minimums occur within this belt: one at a density contrast of 500 kg/m^3 and a maximum depth of 50 km (model M500), and the other at a density contrast of 400 kg/m^3 and a maximum depth of 60 km (model M400). Since the topography of the model space around the two minimums is similar, we consider both cases in the genetic algorithm search. In each case we let the search to go through 100 generations to arrive at a stable solution. Following Silva et al. (2002), we confine the search to the class of compact bodies without holes and complex protrusions (i.e., saw-toothed zigzags on a surface). Protrusions are avoided on the model Moho by requesting

$$H + x = H + 2\,\text{km} \quad \text{if} \quad x \geq 1\,\text{km},$$
$$= H \qquad\qquad \text{if} \quad |x| < 1\,\text{km},$$
$$= H - 2\,\text{km} \quad \text{if} \quad x \leq -1\,\text{km},$$

where H is the Moho depth of the current model. Holes are avoided by requesting that any hole created be filled by the density of the adjacent elements. The revised model is placed back in the genetic algorithm selection process to create the next generation of models.

The average misfits for models M400 and M500 are 3.35×10^{-5} and 3.65×10^{-5} m/s^2 (i.e., 3.35 and 3.65 mGal), respectively. The inverted Moho depth for the two models is overlaid on the outlines of the major structural units in Taiwan and displayed in Figures 7a and 7b. Both models show a crustal
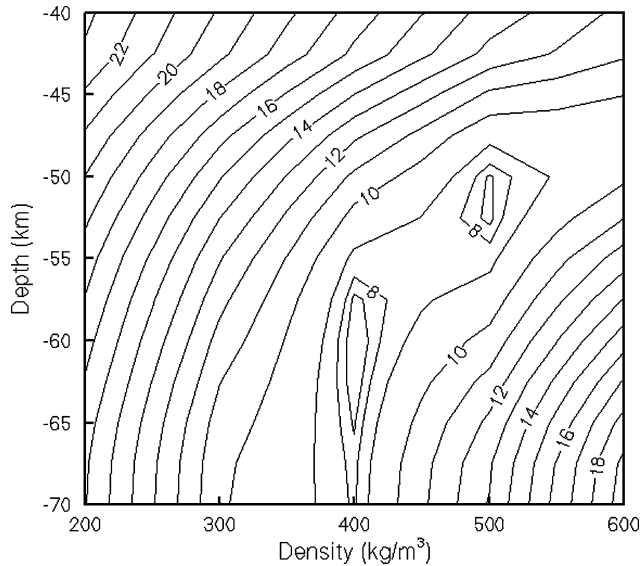

Figure 6. Misfit function (in 10^{-5} m/s^2, or mGal) in model space of Moho density contrast and maximum Moho depth. Note the occurrence of a belt of relative minimum and two local minimums within this belt.

root trending north-northeast–south-southwest beneath the Western Central Range at latitudes below 24°N; these turn northeastward at higher latitudes toward the Eastern Central Range. The calculated gravity anomaly for the two models is given in Figures 8a and 8c, and the difference between the calculated gravity anomaly and the anomaly in Figure 4d are
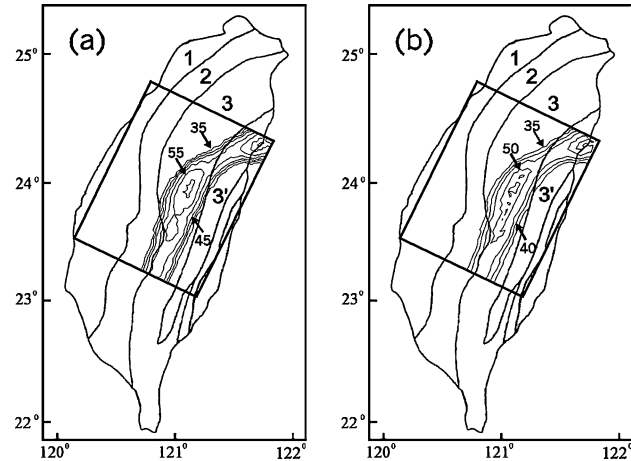

Figure 7. (a) Inverted Moho depth for model M400. (b) Inverted Moho depth for model M500. Numbers on contours are in kilometers below sea level.
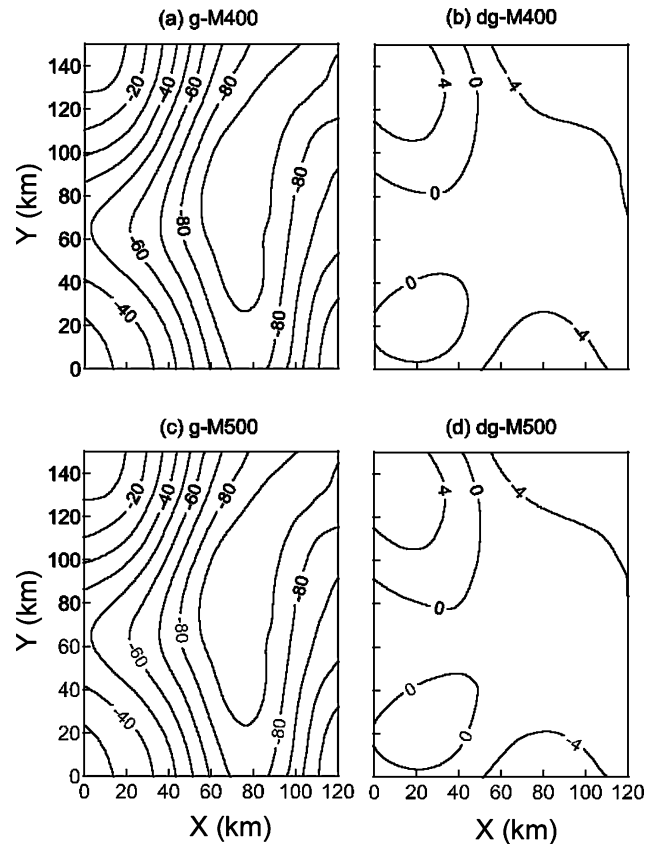

Figure 8. (a) Calculated gravity anomaly for model M400. (b) Difference between residual gravity anomaly (Figure 4d) and (a). (c) Calculated gravity anomaly for model M500. (d) Difference between residual gravity anomaly (Figure 4d) and (c). Numbers on contours are in 10^{-5} m/s^2 (i.e., mGal).

given in Figures 8b and 8d, respectively. Figures 8a and 8c show that both inverted models have recovered the most important feature in the residual gravity anomaly, i.e., an elongated arc of negative gravity anomaly along the Western and Eastern Central Ranges. Figures 8b and 8d show that the maximum difference between the calculated anomaly and the anomaly in Figure 4d is $\sim 5 \times 10^{-5}$ m/s^2 (i.e., $\sim$5 mGal).

Case 2: Density difference in the upper 34 km

Here we assume that the residual gravity anomaly is entirely the result of density differences from the initial model in the upper 34 km, which may arise from the uncertainty in the empirical velocity–density relation and/or in the seismic velocity model. In this case, we use the genetic algorithm to determine the unaccounted density differences, assuming the density below 34 km is laterally uniform. As in the previous case, we examine the misfit function in the model space of the density difference. We construct the misfit function by allowing the density difference $\Delta\rho$ to change from 10 to 600 kg/m^3. The mean of the misfits of the 32 models in the last generation in the genetic algorithm inversion is plotted against the allowed density difference in Figure 9. It shows no local minimum but a continued decline from 45×10^{-5} m/s^2 (i.e., 45 mGal) at $\Delta\rho = 10$ kg/m^3, to 25×10^{-5} m/s^2 (i.e., 25 mGal) at $\Delta\rho = 300$ kg/m^3, and to 19×10^{-5} m/s^2 (i.e., 19 mGal) at $\Delta\rho = 600$ kg/m^3. Thus, a density model in the upper 34 km could be found to satisfy the gravity data only if the allowed density contrast were increased beyond 600 kg/m^3. However, numerical experiments show that if the density contrast equals or exceeds 100 kg/m^3, the inverted density model begins to lose the structural integrity inherited from the seismic tomographic velocity. In other words, if we confine the density anomaly in the upper 34 km and force the model to fit the gravity data, the structural fabrics of the density model would no longer resemble that of the tomographic seismic velocity. Since the structural fabric of the tomographic seismic velocity model needs to be honored, no density model can be found to fit the anomaly if the changes are confined within the upper 34 km.
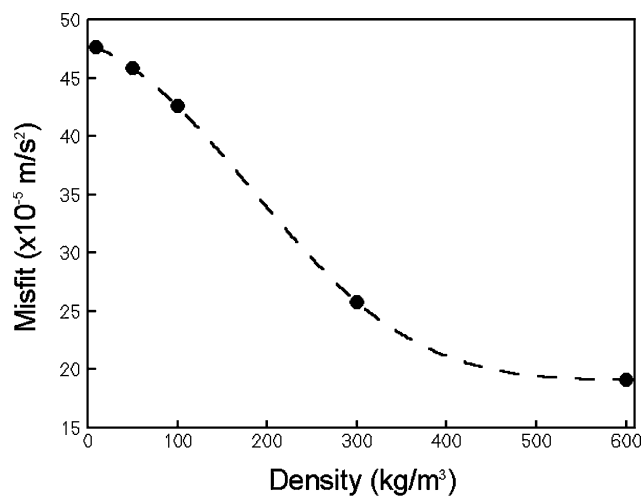

Figure 9. Misfit function (in 10^{-5} m/s^2, or, mGal) plotted against density difference from the initial density model. No relative minimum in misfit function occurs in this space.

DISCUSSION

Tomographic imaging by Rau and Wu (1995) reveals a crustal root extending to 50 km beneath the Central Ranges. Even though the root revealed by seismological means may not necessarily be the same as that revealed by gravity inversion, the seismological finding provides an independent, albeit qualitative, confirmation of the present result. Comparison between Figures 7a and 7b shows that models M400 and M500 are hardly distinguishable on the basis of gravity data alone. This indicates that the current resolving power of the gravity data is insufficient for discriminating between the two models and that independent studies would be needed.

The density contrast of 400 to 500 kg/m^3 across the Moho, predicted in this study from the minimums of the misfit function, is consistent with the available petrophysical data for the density contrast between the major rock type in the lower crust and that in the upper mantle (e.g., Birch, 1961; Christensen and Mooney, 1995); it is also in agreement with the results of independent gravimetric studies on the density contrast across the Moho in other parts of the world (e.g., Lefort and Agarwal, 2002).

Both M400 and M500 show a flat Moho at a depth between 34 and 35 km, except in areas beneath the Central Ranges, in agreement with the result in a 2D model of Wu et al. (1997, their Figure 12). In addition, both models show that the north–northeast-trending root beneath the Western Central Range, at latitudes below 24°N, turns clockwise towards the northeast to lie beneath the Eastern Central Range at higher latitudes. As noted earlier, a major change in the structural trend occurs in Taiwan, from a north-northeast trend in central Taiwan to a northeast trend at higher latitudes (Ho, 1988; Lu et al., 1995). Lu and Malavieille (1994) suggest that the change in the structural trend may represent a rotation of the deformed crustal blocks around the northern tip of the Luzon arc that acts as an indenter in an oblique collision between the Philippine Sea plate and the China continental margin. This interpretation is consistent with the available stress (Lu et al., 1995) and global positioning system (GPS) measurements (Yu et al., 1997), which show similar clockwise rotation in their principal directions. Although both the modeled crustal root and the geologic structure show similar clockwise rotations, the former turns at a lower latitude such that it crosses the boundary between the Western and the Eastern Central Ranges to lie beneath the Eastern Central Range at higher latitudes.

While this result may provide a target for future research, several factors could have contributed to uncertainty in the present result. First, the models examined above represent end-member models. In reality, density difference from the initial model may occur both above and below 34 km, and these may contribute in different proportions to the residual gravity anomaly. Second, the seismographic stations of the Central Weather Bureau seismic network used in Cheng (2000) were all located on land. Thus, the crust in the coastal area was relatively poorly sampled by seismic rays. This may lead to a relatively large uncertainty in the velocity model near the coastal area. Third, laboratory experimental error in determining velocity and density of rocks and the scatter of experimental data suggest there may be substantial uncertainty in the empirical velocity–density relationship (10) and thus considerable uncertainty in the initial density model. Finally and noted earlier,

uncertainty exists in the removal of the regional trend from the gravity data. The result of numerical experiments, however, shows that this uncertainty may not change the major characteristics of the gravity anomaly, even though it may affect the magnitude of the anomaly.

The uncertainties in the seismic velocity model and in the initial density model may cause corresponding uncertainties in the calculated gravity anomaly of the initial density model, which in turn may result in an uncertainty in the residual gravity anomaly used in the genetic algorithm inversion. However, in view of the fact that the misfit function in Figure 9 does not show a local minimum in the model space of the density difference from the initial model, we believe that the uncertainties noted above may not change the conclusion of the present study that the major cause of the residual gravity anomaly is a low-density crustal root beneath the Central Ranges extending from 34 km to depth of 50 to 60 km.

ACKNOWLEDGMENTS

REFERENCES

Angelier, J., Barrier, E., and Chu, H.-T., 1995, Plate collision and paleo-stress trajectories in a fold-thrust belt: The foothills of Taiwan: Tectonophysics, **125**, 161–178.

Bathe, K.-J., 1996, Finite element procedures: Prentice-Hall, Inc.

Birch, F., 1961, The velocity of compressional waves in rocks to 10 kilobars, part 2: Journal of Geophysical Research, **66**, 2199–2224.

Blakely, R. J., 1995, Potential theory in gravity and magnetic applications: Cambridge University Press.

Camacho, A. G., Montesinos, F. G., and Vieira, R., 2002, A 3-D gravity inversion tool based on exploration of model possibilities: Computers & Geosciences, **28**, 191–204.

Cheng, W. B., 2000, Three-dimensional crustal structure around the source area of the 1999 Chi-Chi earthquake in Taiwan and its relation to the aftershock locations: Terrestrial Atmospheric and Oceanic Sciences, **11**, 643–660.

Christensen, N. I., and Mooney, W. D., 1995, Seismic velocity structure and composition of the continental crust: A global view: Journal of Geophysical Research, **100**, 9761–9788.

Dobrin, M. B., and Savit, C. H., 1988, Introduction to geophysical prospecting, 4th ed., McGraw-Hill Book Company.

Goldberg, D.E., 1989, Genetic algorithm: Addison-Wesley Publ. Company.

Goldberg, D. E., and Richardson, J., 1987, Genetic algorithm with sharing for multimodal function optimization: 2nd International Conference on Genetic Algorithm, Proceedings, 41–49.

Hjelt, S.-E., 1992, Pragmatic inversion of geophysical data: Springer-Verlag Berlin.

Ho, C. S., 1988, An introduction to the geology of Taiwan: Explanatory text for the geologic map of Taiwan, 2nd ed: Republic of China, Ministry of Economic Affairs.

Humphreys, E., and Clayton, R.W., 1988, Adaptation of back projection tomography to seismic travel time problems: Journal of Geophysical Research, **93**, 1073–1085.

Johnson, L. R., and Litehiser, J. J., 1972, A method for computing the gravitational attraction of three dimensional bodies in spherical or ellipsoidal earth: Journal of Geophysical Research, **77**, 6999–7009.

Lefort, J. P., and Agarwal, B. N. P., 2002, Topography of the Moho undulations in France from gravity data: Their age and origin: Tectonophysics, **350**, 194–213.

Lu, C.-Y., and Malavieille, J., 1994, Oblique convergence, indentation and rotation tectonics in the Taiwan mountain belt: Insight from experimental modeling: Earth and Planetary Science Letters, **121**, 477–494.

Lu, C.-Y., Angelier, J., Chu, H.-T., and Lee, J.-C., 1995, Contractional, transcurrent, rotational and extensional tectonics: Examples from northern Taiwan: Tectonophysics, **246**, 129–146.

Mansanne, F., and Schoenauer, M., 2002, An automatic geophysical inversion procedure using a genetic algorithem, *in* Wong, P., Aminzadeh, F., and Nikravesh, M., Ed., Soft computing for reservoir characterization and modeling: Physica-Verlag, Heidelberg, 331–353.

Oldenburg, D. W., 1974, The inversion and interpretation of gravity anomalies: Geophysics, **39**, 526–536.

Parker, B. P., 1999, Genetic algorithms and their use in geophysical problems: Ph.D. thesis, University of California at Berkeley.

Parker, R. L., 1972, The rapid calculation of potential anomalies: Geophysical Journal of the Royal Astronomical Society, **31**, 447–455.

Rau, R. J., and Wu, F. T., 1995, Tomographic imaging of lithospheric structures under Taiwan: Earth and Planetetary Science Letters, **133**, 517–532.

Shi, Y., 1992, Genetic algorithm and some of its geophysical applications: Acta Geophysica Sinica, **35**, 367–371.

Silva, J. B. C., Medeiros, W. E., and Barbosa, V. C., 2002, Practical applications of uniqueness theorems in gravimetry: Part I—Constructing sound interpretation methods: Geophysics, **67**, 788–794.

Suppe, J., 1987, The active Taiwan mountain belt, *in* Schaer, J. P., and Rodgers, J., Ed., The anatomy of mountain ranges: Princeton University Press, 277–293.

Talwani, M., Worzel, J. L., and Landisman, M., 1959, Rapid computation for two-dimensional bodies with application to the Mendocino submarine fracture zone, Journal of Geophysical Research, **64**, 49–59.

Teng, L. S., 1990, Geotectonic evolution of late Cenozoic arc-continent collision in Taiwan: Tectonophysics, **183**, 57–76.

Tsai, K.-C., 1999, Study of gravity trrain correction (in Chinese): Master's thesis, National Central University, Taiwan.

Wu, F. T., Rau, R.-J., and Salzberg, D., 1997, Taiwan orogeny: Thin-skinned or lithospheric collision?: Tectonophysics, **274**, 191–220.

Yen, H.-Y., Yeh, Y.-H., Lin, C.-H., Chen, K.-J., and Tsai, Y.-B., 1995, Gravity survey of Taiwan: Journal of Physical Earth, **43**, 685–696.

Yu, S.-B., Chen, H. Y., and Kuo, L.-C., 1997, Velocity field of GPS stations in the Taiwan area: Tectonophysics, **274**, 41–59.

Zienkiewicz, O. C., and Taylor, R. L., 1988, The finite element method: McGraw-Hill: Book Company.